Mechanism of pH sensing in the human voltage-gated proton channel hHv1

Yandong Huang[1,*], Zhitao Cai[1], Tengzi Liu[1], and Jana Shen[2,*]

[1]College of Computer Engineering, Jimei University, Xiamen 361021, Fujian Province, China
[2]Department of Pharmaceutical Sciences, University of Maryland School of Pharmacy, Baltimore, MD 21201
[*]yandonghuang@jmu.edu.cn,jana.shen@rx.umaryland.edu

ABSTRACT

The voltage-gated proton channel Hv1 is indispensable for preserving physiological pH in cells and is characterized by distinct pH dependence. However, the mechanism of how Hv1 is regulated by pH is still obstacle. Under the framework of simulated hyperpolarized and depolarized states, continuous constant-pH molecular dynamics simulations have been performed to explore the coupling between conformational activation and protonation equilibra of the human Hv1. As a result, we identify E196 as the external pH sensor that works synchronously with the putative internal pH sensor H168. Further D174 is found to play a central role during the activation. Based on the pK_a splitting between H140 and H193, we propose a pH-dependent mechanism of inhibitive Zn^{2+} binding to the external vestibule. Finally, our results offer an explanation of the measured threshold voltage shifts in response to the neutralizing mutations, including D174 above and three putative gating charges R205, R208 and R211, shedding light on the relationship between structure and function of the human Hv1.

Introduction

The voltage-gated proton channel (Hv1) belongs to a super family of proteins which become activated through a voltage-sensing domain[1,2]. However, unlike voltage-gated sodium or potassium channels, Hv1 does not possess a separate pore domain and it is also gated by pH[3,4]. Hv1 functions primarily by extruding protons from cells to maintain the fundamental pH homeostasis in cells and also involves in many biological events, such as reactive oxygen species (ROS) production[5], sperm mobility[6] and B-cell activation[7], making it a competitive target for drug design[8,9]. The responses of wild-type Hv1 and its mutants to membrane potential and pH gradient have been investigated extensively to locate the residues essential for Hv1 activation and the subsequent proton conduction since it was first identified in 2006[1,10]. For instance, in contrast to other alanine substitutions, threshold voltage deviates significantly from that of the human Hv1 (hHv1) by mutating the highly conserved D174[11]. In addition, neutralizing mutation of R211, one of the three putative gating charges in hHv1, gives considerable change of the threshold voltage from that of the wild type[11]. However, the underlying mechanisms are still unclear.

To interpret the perturbation of a selected mutation to the function, a high-resolution crystal structure of Hv1 is fundamental. At present two crystal structures of Hv1 are available[12,13]. One is a chimeric construct of the mouse proton channel mHv1cc[12] and the other is a solution NMR structure of the voltage-sensing domain of hHv1 embedded in mixed detergent micelles[13]. However both of them correspond to the inactive state. As to the open state of Hv1, people turn to computational schemes. Because of high sequence similarity of the voltage-sensing domain between Hv1 and other voltage-gated cation channels, the structure of a potassium or a sodium channel was often taken as the template to model the open state of Hv1[11,14–19]. A sodium or potassium channel owns a separate pore domain for ion transfer, whereas protons are conducted by the same voltage-sensing domain. Thus, such a template-based modeling of the open state might not work for proton permeation. Alternatively, experimental constrains derived from EPR spectra have been applied to the structural refinement of the model built on CiVSD-WT[20]. Though a promising protocol, the structure obtained is the resting state of the human Hv1 (hHv1), asking for a bottom-up prediction of the open state by theory.

The conformational transition of hHv1 from the putative closed to open states has been exploited by molecular dynamics (MD) simulations recently where extra electric field[21] or pH gradient[22] across the membrane was considered implicitly to accelerate the gating kinetics. To overcome the underlying obstacle of non-native proton permeation pathway, mHv1cc crystal structure was taken as the template to construct the closed state of hHv1 or initial structure of MD simulations[12,21]. The pH gradient was realized by the discrete protonation-state constant pH molecular dynamics (DpHMD) method that employs generalized Born-based implicit solvent to account for mean solvent effect[23]. We note that to elucidate the conformational activation induced by pH gradient, accurate pK_a estimation that determines the protonation equilibrium is of importance. Nevertheless, under the continuum dielectric approximation, the implicit solvent used by DpHMD is limited to soluble

proteins[24]. As to a channel embedded in a lipid bilayer, more sophisticated approach is desired. On the other hand, it has been pointed out mutant channels generate robust H+ currents as long as a big enough voltage is offered[11]. To mimic the physiological hyperpolarization and depolarization of the cellular membrane, extra electric-field forces in the opposite directions were applied to the charges in the pore during the MD simulation[21]. As a result, the closed- and open-state models were obtained and validated. To emphasize the source of driving force, here and after the modeled voltage-triggered closed and open states are named hyperpolarized and depolarized states respectively. As illustrated in Fig. 1, the voltage-sensing domain of hHv1 in the hyperpolarized (Hyperpol) and depolarized (Depol) states are displayed with the new cartoon model. To understand the displacements, -5.2, -1.7, -3.7 and 8.9 Å (Tab. S1), of four transmembrane helices S1 to S4 respectively at z direction in response to the depolarization of the membrane potential from hyperpolarization, acidic (Asp and GLu) or basic residues (His, Lys and Arg) that are at least one helix loop away from the helix terminals are defined as the pore residues (See Fig. 1). Given the default charge states (Asp(-), Glu(-), His(0), Lys(+) and Arg(+)) at neutral pH of these pore residues[21], the net charges in the pore domains of S1-S4 are -2, 0, -2 and 3 (e) respectively (Tab. S1), which to some extend explains the downward and upward displacements of S1-S3 and S4 respectively. In addition, the net charges of intracellular and extracellular sides are +7 and -2 (e) respectively (Tab. S1), creating an inner electric field which might be large enough to have the hHv1 activated and therefore explain the spontaneous activation of hHv1 in the absence of voltage and pH gradient[25].

A recent experimental study revealed that hHv1 owns distinct internal and external pH sensors[26]. In particular, H168 was identified as the internal pH sensor, however the external pH sensor is still elusive. Besides, the molecular mechanism of how Hv1 is regulated by pH is to be answered. Thus, the above simulated hyperpolarized and depolarized states of monomeric hHv1 offer the framework of investigating the coupling of protonation equilibra with the conformational activation for the present work. The membrane-enabled continuous protonation-state constant pH molecular dynamics (CpHMD) method[27] has been successfully applied to exploring the proton-coupled conformational dynamics of membrane proteins, including the sodium-proton antiporter NhaA[27,28], proton channel M2[29], multidrup pump AcrB[30], and μ-opioid receptor mOR[31]. In this work, CpHMD simulations that start from the hyperpolarized and depolarized states of the monomeric hHv1 respectively were carried out to study the titration in response to the activation. Noting that the pH-gradient dependence is not eliminated by single point mutations of titratable sites, the pH gradient is more likely a potential, like the voltage that drives gating[10,11,32]. Besides, it's pointed out that the rate of Hv1 channel opening relies on the internal and external pH values instead of the pH gradient[33]. Thus, either pH gradient or voltage can be removed from the simulation, so that one can focus on pH sensing. Apart from an independent function unit[34], monomeric Hv1 has been proved a suitable model for investigating the channel pH dependence[33], supporting the monomeric structure of hHv1 utilized in the present CpHMD simulations.

Our study suggests that E196 is the external pH sensor, which is coupled with the internal pH sensing nearby the physiological pH. A simplified salt bridge-based model, where the salt bridge D174-R211 plays a key role, is proposed to elucidate the gating kinetics and statistics, validating the three-click drifting of S4 in response to depolarization[21]. Once hHv1 is activated, we found that protonation of D174 triggers the putative hydrophobic gasket[35] wide opening. hHv1 channels can be inhibited effectively by presumably a pair of Zn^{2+} ions that bind to the external vestibule and stabilize the hHv1 voltage-sensing S4 at resting conformations[13,36–38]. However, it's unclear whether the binding of Zn^{2+} is pH dependent too. Based on the calculated pK_a's of the two primary Zn^{2+} binding sites H140 and H193[1,12,39], we come up with a pH-regulated mechanism of Zn^{2+} binding. Lacking high resolution open-channel Hv1 structures, the mechanism of proton transfer is still controversial[40,41]. The debate mostly refers to whether the H^+ permeation requires transient protonation of an acid, presumably D112 at the central crevice[4,40,42], or a water wire is available for Grotthuss-type proton transfer[11,41,43]. The first view emphasizes the titration of D112. However our pK_a estimation of D112 suggests that it's deprotonated or charged nearby the physiological pH. Finally, it should be pointed out that the hypotheses regarding the proton transfer and Zn^{2+} binding are quite preliminary and explicit simulation of Zn^{2+} binding or proton transfer is demanded for more details.

Results

From the CpHMD simulations of the human proton channel hHv1, we have decoded three conserved residues, namely H140, H168 and E196, the pK_a's of which vary by more than 1.0 pH unit when the conformation is activated from the hyperpolarized to the depolarized state. Such pK_a differences imply the coupling between titration and conformational dynamics, which will be elucidated in details below. Besides, the pK_a shifts of D174 and H193 from the reference values in both states are over 1.5 pH units, indicating specific electrostatics that might be associated with the function.

Taking into account the putative closed and open states triggered by hyperpolarized (+150 mV) and depolarized (+150 mV) membrane potentials respectively[21], the structure would converge back to the initially unpolarized state in the absence of electric field (0 mV), which might call for another ten-microsecond-timescale simulation. As a matter of fact, the present work aims to see if there is any difference in titration between the closed and open models provided by long-timescale MD simulations, implying that the pK_a's that reflect local fluctuations in structure are sufficient. To demonstrate the pK_a's derived from CpHMD simulations, especially for the residues with slow pK_a convergences, such as the H168, any conformational

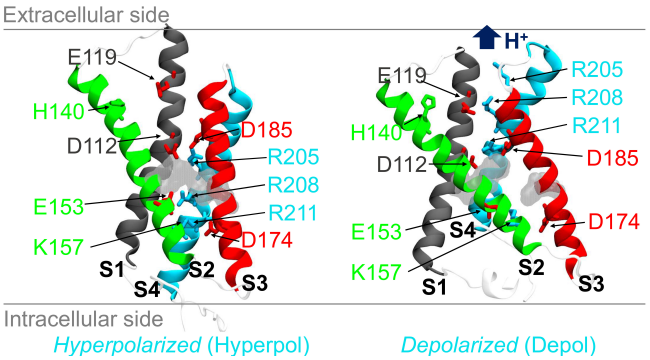

Figure 1. Hyperpolarized- (left) and depolarized-state (right) models of hHv1[21]. Four transmembrane helices S1 (gray), S2 (green), S3 (red) and S4 (cyan) are represented by the new cartoon model. Pore-lining residues displayed with the stick model are highlighted using the same colors with the helices they belong to. The putative hydrophobic gasket, composed by V109, F150, V177 and V178[35], is represented by the transparent surface rendering. Hyperpol and Depol in the parentheses are the abbreviations of hyperpolarized- and depolarized-state models respectively. Images are made with VMD.

change that perturbs the protonation equilibra and the resulting pK_a's has been assessed by comparing with the reference structures of the hyperpolarized (closed) and depolarized (open) states respectively. In addition, two independent rounds of CpHMD simulations give consistent pK_a's, supporting the pK_a changes or shifts mentioned above. Unless otherwise noted, the discussion below refers to the first round. Convergence analyses of pK_a's are given in the supporting information (Fig. S1).

pH$_i$ sensor H168 disturbs hydrophobic gasket opening by deprotonation

pK_a's of H168 in the hyperpolarized and depolarized states are 5.0 and 6.8 respectively, which means deprotonated or neutral state of H168 is more favored by the hyperpolarized state (Fig. 2A). H168 has been identified as the pH$_i$ sensor by Thomas E. DeCoursey's group and it's pointed out that the activation kinetics of hHv1 can be accelerated by its mutant H168X where X stands for T, S and Q, which are characterized as neutral and hydrophilic[26]. Interestingly, pH$_i$ responses of wild type (WT) and H168X converge at pH$_i$=6.0 as pH$_i$ decreases from 9.0 to 5.0[26]. Thus, it's likely that the gating kinetics of wild-type hHv1 is slowed down by the deprotonation of H168, supporting the depressed pK_a's derived from the CpHMD simulation of the hyperpolarized state. To interpret the pK_a difference above, the interactions that could influence the pK_a shifts of H168 have been computed. From the minimal distance between H168 sidechain and C atoms of lipid tails ($r_{\mathrm{lipid:C-H168}}$) as a function of pH, one can tell that the hydrophobic interaction between H168 and lipids is stronger in the hyperpolarized state. Second, based on the hydration number (N_{hydr}) of H168 sidechain oxygens, H168 is more buried in the hyperpolarized state. According to the intermolecular interactions of H168 with lipids and aqueous solvent above, neutral state of H168 is more stable in the hyperpolarized state than that in the depolarized state. Next, the number of hydrogen bonds (N_{HBonds}) that H168 takes part in as the donor was calculated. It's evident that N_{HBonds} in the hyperpolarized state is about 0.5 smaller than that in the depolarized state, indicating that the protonated state of H168 is less stable in the hyperpolarized state. Two typical hydrogen bonding modes that correspond to deprotonated and protonated H168 respectively are extracted from the CpHMD simulation of the hyperpolarized state and displayed in Fig. 2B. When H168 is neutral (H168(0)), its sidechain involves in two hydrogen bonds with the backbone oxygens of R162 and E164 respectively. As to the protonated H168 (H168(+)), sidechain carboxyl oxygens of E164 and D171 and backbone oxygen of E164 form three hydrogen bonds with H168. From the minimal distances from H168 to F161 ($r_{\mathrm{F161-H168}}$) and R162 ($r_{\mathrm{R162-H168}}$) sidechains, imidazole ring of H168, especially when H168 is deprotonated at a higher pH condition, is able to form π-π and π-cation stacking with F161 and R162 respectively[44]. Remarkably, the π-cation contact between R162 sidechain and deprotonated imidazole ring of H168 can be stabilized by two salt bridges contributed by R162 sidechain and carboxyl oxygens of E164 and E171 sidechains (Fig. 2B H168(0)). Even when H168 is protonated, less compact π-cation stacking between H168 and F161 sidechains could be observed[44]. Thus a salt bridge-aided sandwish-like stacking can be identified (Fig. 2C), which is special for deprotonated H168 as the indispensable imidazole ring is unique among 20 amino acid types. It has been shown in experiment that H168X mutants accelerate activation 10-fold and attenuate the pH$_i$ response significantly[26]. Here we propose that such an imidazole ring-centralized stacking mode is critical for slowing down gating kinetics of hHv1. From the minimal distance calculations, no interaction is found between H168 and its immediate neighbors, F165, F166 and H167 (Fig. S2), consistent with the experiments that pH$_i$ responses of mutants F165A, F165H, F166L, and H167K are close to that of WT when compared with that of H168X[26].

It's worth noting that F161 and R162 belong to S2–S3 linker and is close to the inner end of S2, whereas H168 belongs to S3 and locate at the inner end of S3. Thus, the displacement of S3 relative to S2, if any, could be hindered by the sandwish-like

stacking mentioned above. Indeed, from Fig. 2D based on the CpHMD simulation of the hyperpolarized state, it's obvious that the titration coordinate of H168 (λ_{H168}) is coupled with the displacement of S3 at z direction (Z_{S3}). For instance, when H168 is fully deprotonated ($0.8<\lambda_{H168}<1.0$) at pH=8, S3 stays in the hyperpolarized state. Whereas, when the protonated state ($0.0<\lambda_{H168}<0.2$) is sampled at pH=5, S3 drifts down to the depolarized state. Recently, the hydrophobic gasket of hHv1 was identified as V109 in S1, F150 in S2, V177 and V178 in S3[35]. Therefore, the minimal distance between F150 and V177/V178 sidechains ($r_{V177/178-F150}$) was calculated. As illustrated in Fig. 2E, $r_{V177/178-F150}$ (x-axis) is distributed around 4.0 Å at pH=8.0 (state a), reflecting intact hydrophobic interaction between F150 and V177/178 as observed in the hyperpolarized state (Fig. 1). As pH reduces to 5, a minor distribution (state b) with a larger $r_{V177/178-F150}$ of around 7.0 Å emerges, resembling the absence of hydrophobic contact between F150 and V177/178 in the depolarized state (Fig. 1). Radius of gyration (R_g) is often used to measure how open a hydrophobic gasket is[27]. From Fig. 2E, it's evident that R_g is positively related with $r_{V177/178-F150}$, implying that $r_{V177/178-F150}$ can be utilized to represent the openness of the hydrophobic gasket. From the correlation plot between $r_{V177/178-F150}$ and Z_{S3}, especially when pH equals 5, one can tell that Z_{S3} is negatively related with $r_{V177/178-F150}$. Here we suggest that the sandwish-like stacking above controls the dynamics of the hydrophobic gasket via the displacement of S3 at z direction or membrane normal. For instance, when H168 is deprotonated (H168(0)), the sandwish-like stacking is maintained, which hinders S3 drifting down. The up state of S3 as in the hyperpolarized state facilitates the hydrophobic interaction between F150 and V177/178. As a result, the closed state of the hydrophobic gasket is stabilized (Fig. 2F). Once H168 is protonated (H168(+)), the sandwish-like stacking is disrupted, which allows S3 to move downwards and the resulting hydrophobic gasket opening (Fig. 2G).

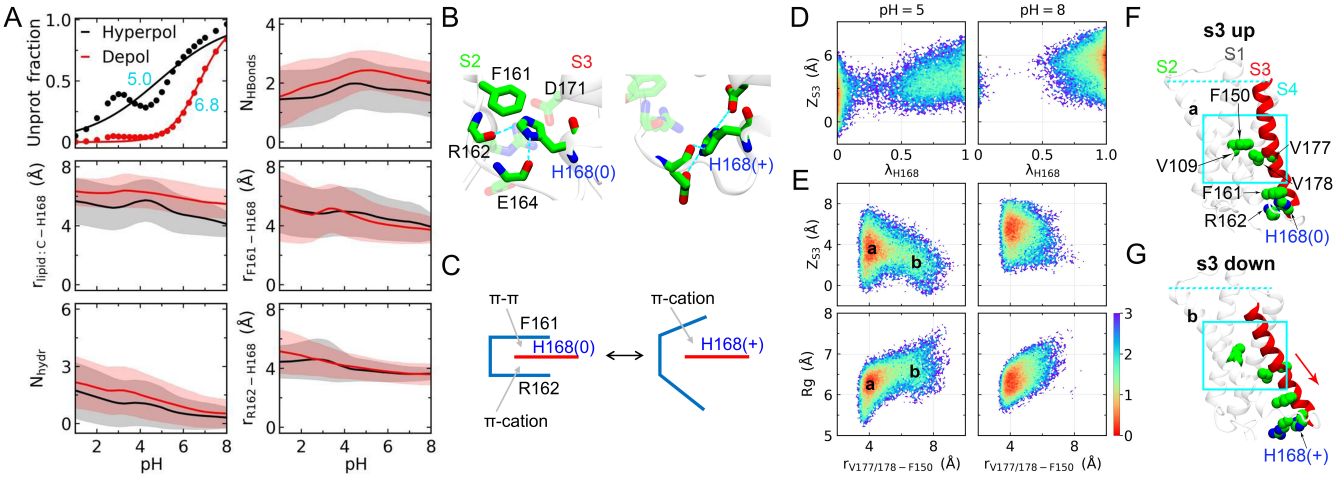

Figure 2. Titration of H168 is coupled with the hydrophobic gasket. (A) Unprotonation fraction of H168, minimum distance between H168 sidechain and lipid tail carbons ($r_{lipid:C-H168}$), hydration number of H168 (N_{hydr}), the number of hydrogen bonds involved by H168 as the donor (N_{HBonds}), the minimum sidechain distances between F161 and H168 ($r_{F161-H168}$) and between R162 and H168 ($r_{R162-H168}$) as a function of pH for hyperpolarized (black) and depolarized (red) states. The two titration curves were obtained by fitting the data points (solid cycles) to the generalized Henderson-Hasselbalch equation. pK_a values of H168 in the hyperpolarized (5.0) and depolarized (6.8) states are shown. Standard deviations are displayed with shadows. Hydrogen bonds were defined using a donor-acceptor distance cutoff of 2.4 Å[45]. (B) Two snapshots showing the hydrogen bonds (dash cyan) formed by deprotonated (left) and protonated (right) H168. Residues are represented with the stick model. (C) Simplified cartoons showing the π-π and π-cation stackings of deprotonated H168 with F161 and R162 respectively (left) and the π-cation stacking between H168 and F161 when H168 is protonated (right). (D) Correlation between titration coordinate of H168 (λ_{H168}) and z-axis position of helix S3 (Z_{S3}) at pH=5 (left) and 8 (right). (E) Correlations between the minimum sidechain distance between F150 and V177/V178 ($r_{V177/178-F150}$) and Z_{S3} and between $r_{V177/178-F150}$ and radius of gyration of the hydrophobic gasket (R_g) at pH=5 (left) and 8 (right). The probability density was converted to relative free energy ΔG calculated by $-RT\ln(n_{ij}/N)$, where R is the Boltzmann constant, T denotes room temperature of 310 K, n_{ij} is the number of data points in the bin, and N is the total number of data points collected in the entire region. Two snapshots that show (F) the original S3 up and (G) newly sampled S3 down states are represented with the new cartoon mode. Downward displacement of S3 is represented by a red arrow. Residue sidechains are displayed with the vdW surface mode. The hydrophobic gasket is encompassed by a frame in cyan. A dashed cyan baseline is used to probe the displacement of S3.

E196 is identified as the pH_o seneor

To identify the pH_o seneor, we turn to the calculated pK_a's of extracellular side residues. It's found that pK_a's of E196 in the hyperpolarized and depolarized states are 7.5 and 4.0 respectively (Fig. 3A). Such a pK_a deviation of 3.5 pH units makes E196 a potential pH_o seneor. E196 locates at the outer end of S4 and is isolated, thus the minimal distance between sidechain oxygens and lipid tail carbons ($r_{lipid:C-E196}$) was calculated (Fig. 3B) to explain the pK_a split between the two states. Apparently, E196 interacts with hydrophobic lipid tails in the hyperpolarized state and therefore the protonated state is preferred (E196(0) in Fig. 3C). In contrast, the interaction between E196 and lipid tails is weakened significantly in the depolarized state, implying that E196 is likely to be exposed to water and charged (E196(-) in Fig. 3C). From the hydration number (N_{hydr}) of sidechain oxygens as shown in Fig. 3D, it's evident that E196 is highly buried in the hyperpolarized state, in agreement with the $r_{lipid:C-E196}$ data above. From Fig. 3E by the CpHMD simulation of hyperpolarized state, protonation of E196 (λ_{E196}) is positively related with the displacement of S4 at z direction (Z_{S4}), the trend of which is consistent with the conformational transition of S4 from hyperpolarized (Z_{S4}=-3.0Å) to depolarized states (Z_{S4}=5.9Å) (Tab. S1). Now that the conformational changes regarding S3 and S4 are obtained by the same CpHMD simulation initialized from the hyperpolarized state, it's of interest to see whether the displacement of S4 is coupled with that of S3. Encouragingly, from the anti-cross correlation $R(\lambda_{E196} - \lambda_{H168})$ based on the CpHMD simulation of hyperpolarized state, the titration coordinates of E196 and H168 are negatively related at pH=7, implying negative cooperativity between Z_{S4} and Z_{S3}. Our study suggests that E196 is the pH_o sensor and its neutralization hinders the conformational activation of S4, which is associated with the displacement of S3 mediated by the titration of putative pH_i sensor H168. As illustrated in Fig. 3G, S3 and S4 drift downwards and upwards respectively, when both H168 and E196 are charged. Notably, an observable anti-cross correlation requires protonated H168 and deprotonated E196 coexisting at a specific pH window, like pH=7. The plots of $R(\lambda_{E196} - \lambda_{H168})$ at different pH conditions can be found in Fig. S3, from which one can clearly see that anti-cross correlation is present only in a narrow pH window around 7.

To comprehend the relative displacement between S3 and S4 above, conformation-specific pK_a's of H168 and E196 were calculated. Obviously the pK_a value of H168 or E196 after the displacements of S3 and S4 is close to that in the depolarized state (Fig. S4), implying that the relative displacement between S3 and S4 is a rate-limiting step to the activation of hHv1. Thus we postulate that the new conformation sampled by the CpHMD simulation initialized from the hyperpolarized state is an intermediate state of hHv1.

pH-dependent salt bridge R211-D174 is crucial for the conformational activation of S4

To understand the conformational activation kinetics and statistics of S4, we place the focus on the calculated pK_a's of acidic residues D112, E119, D123, E153, D174, D185 and E192 that involve in salt bridges with the three putative gating charges R205, R208 and R211 in S4[21]. It's found that the pK_a's of these acids are close to the standard pK_a's, except for D174, the pK_a of which shifts down by over 1.0 pH unit in both states. From Fig. 4, it's noticed that the salt-bridge probabilities P(Salt bridge) are pH independent nearby the physiological pH ranging from 5 to 8, except for R211-D174 in the hyperpolarized state (Fig. 4A). When pH is above 6.5, P(Salt bridge) of R211-D174 is higher than 0.5. Under the pH that ranges from 5 to 6.5, P(Salt bridge) becomes lower than 0.5. Here we assume that a stable salt-bridge interaction is present if P(Salt bridge) is above 0.5. As a result, the number of salt bridges in the hyperpolarized state can be 2 (5<pH<6.5) or 3 (6.5<pH<8), reflecting pH dependence (Fig. 4A). On the other hand, the number of salt bridges in the depolarized state is 4 (Fig. 4B).

It's found that D112 and D185 form stable salt bridges with a single R211 in the depolarized state (Fig. 4B). Thus, it's of interest to see if one of them is capable of donating a proton under the physiological pH conditon by calculating apparent pK_a's (4). From the macroscopic pKa values (pKa_1 and pKa_2), one can see that no proton is released by either D112 or D185 when the pH is 6.5 or higher. According to pKa_2, a proton is supposed to be released, presumably from D185, at a lower pH around 4.0, implying that a proton shuttle might be desired under the intermediate pH condition (3<pH<5). It has been pointed out that D112 is critical for proton selectivity in hHv1[4], which requires D112 a proton shuttle. Nevertheless, our simulations show that D112 forms stable salt bridges in both hyperpolarized (R205-D112) and depolarized (R211-D112) states at pH above 5. Thus we suggest that D112 is more likely a key component for the stabilization of S4 in either hyperpolarized or deopolarized state nearby physiological pH (5<pH<8).

Now that pK_a's of D174 (1.1) in the hyperpolarized state is far below 6.5 (Tab. S2), the pH-dependece of R211-D174 is more likely a result of the conformational change of S3 or S4 as mentioned above (Fig. S5). Thus, we suggest that the conformational activation of S4 is irrelevant to the titrations of these acids at pH ranging from 5 to 8. As illustrated in Fig. 4C, a simplified salt bridge-based model is proposed to explain the pH-dependent activation nearby the physiological pH condition. Here the integers 2 (5<pH<6.5) and 3 (6.5<pH<8) in the hyperpolarized state and 4 (5<pH<8) in the depolarized state indicate the counts of salt bridges that reflect the stability of S4. Obviously, the presumed activated state (S4 up) with 4 salt bridges is the most stable. Thus the reaction progresses from the presumed resting (S4 down) to the activated state (S4 up) is guaranteed. When pH is higher than 6.5, there are 3 salt bridges in the hyperpolarized state, implying an energy barrier of breaking three salt bridges. If the pH is below 6.5 where the R211-D174 salt bridge is removed, 2 salt bridges remain in the hyperpolarized

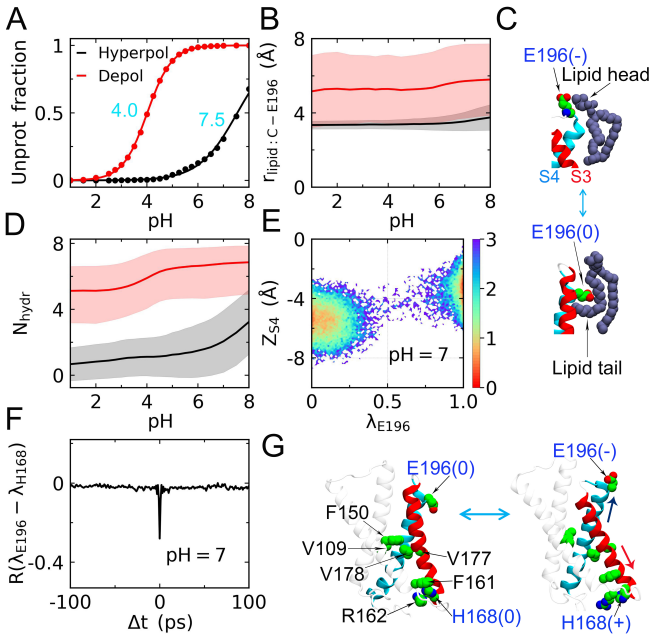

Figure 3. Titration of E196 is coupled with S4. (A) Unprotonation fractions of E196 in the hyperpolarized (black cycles) and depolarized (red cycles) states as a function of pH. The two titration curves were obtained by fitting the data points (solid cycles) to the generalized Henderson-Hasselbalch equation. pK_a values of E196 in the hyperpolarized (7.5) and depolarized (4.0) states are displayed. (B) Minimum distance between E196 sidechain and lipid tail carbons ($r_{lipid:C-E196}$) as a function of pH. (C) Two snapshots showing the interactions between deprotonated E196 and lipid head groups and between protonated E196 and lipid tail groups. (D) Hydration number of E196 in the hyperpolarized (black) and depolarized (red) states as a function of pH. (E) Correlation between titration coordinate of E196 and the z-axis position of S4 at pH=7. (F) cross-correlation of titration coordinates between H168 and E196 $R(\lambda_{E196} - \lambda_{H168})$ at pH=7. (G) Two snapshots showing the structure of the original hyperpolarized state (left) and the conformation (right) where S3 and S4 move down and up respectively when both H168 and E196 are charged (E196(-) and H168(+)). Two arrows are used to indicate the moving directions of S3 and S4.

state, leading to less stable resting state. As a result, the reaction tends to process to the activated state more. At the meantime the activation energy is reduced, making the reaction faster.

Next, previous neutralizing mutations of R205, R208 and R211 are used to demonstrate the importance of removing R211-D174 during the conformational activation of S4. The salt-bridge network of the hyperpolarized state is illustrated in Fig. 5A where R211-D174 as well as R205-D185 is excluded. Assuming that the structure is intact regardless of the mutation, the salt-bridge networks for the wide type (WT) and three single mutants can be represented with simplified cartoons in Fig. 5B. The electric field force on a gating charge is approximated by the gating charge multiplied by presumably uniform electric field intensity contributed partially by the external voltage. Thus the total electric field force acting on S4 can be described by the linear-related number of gating charges (N_Q). Based on the salt bridge-based model, to activate hHv1, the electric field force need overcome the salt bridges. Likewise, the total salt-bridge force that act as a resistance of activation can be described by the number of salt bridges (N_{SB}). Assuming that the forces above have the same magnitude and can be nondimensionalized, the gating charges and salt bridges marked by plus symbols and dashed lines respectively in Fig. 5B are counted to present the forces and recorded to the table of Fig. 5C. ΔN that equals N_Q minus N_{SB} is the net force acting on S4. V_{thr} that denotes the threshold or activation voltage is given in literature[1,11]. Based on the uniform electric field approximation, the relationship of the total electric field force (F) with N_Q and V_{thr} can be formulated as $F=N_QQ(V_{thr}/d)$, where Q and d denote the charge of a protonated arginine and membrane thickness respectively. It's evident that all ΔN values are 1 except for R211A, suggesting that a larger V_{thr} is required to activate R211A mutant of hHv1. Indeed, the experimental V_{thr} for R211A is 77 mV, much higher than that for WT (7 mV), R205 (6 mV) or R208A (14 mV)[1,11]. Eventually, a linear function (eq. 1) can be derived from the linear regression fitting to the two data sets of ΔN and V_{thr} as listed in Fig. 5C. We note that if R211-D174 is intact, then the values of ΔN are zero for all the four situations, giving no correlation with the measured threshold voltages.

$$V_{thr} = -68\Delta N + 77. \quad (1)$$

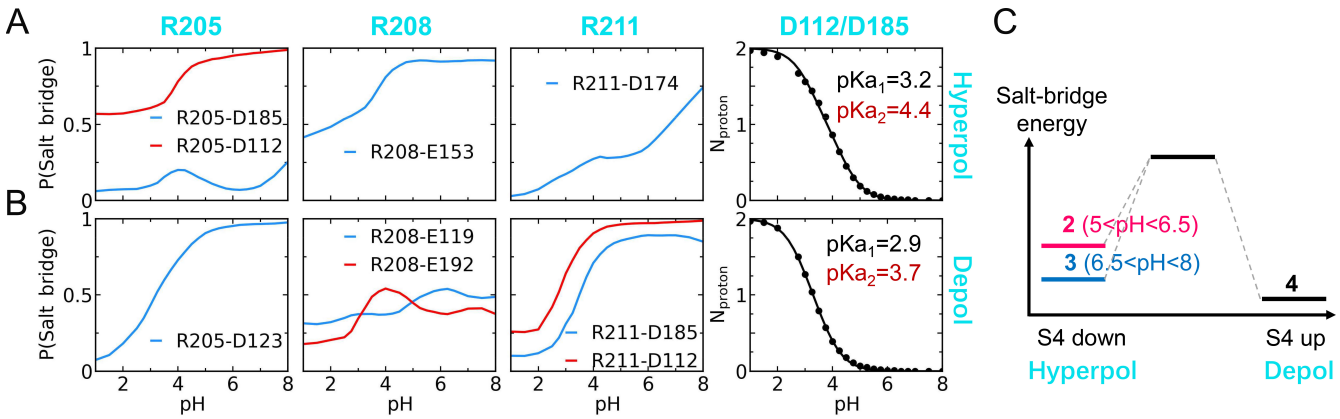

Figure 4. Salt-bridge network in the pore. The probablities of salt bridges involved by R205, R208 and R211 and the number of protons (N_{hydr}) released by the acidic dyad D112 and D185 as a function of pH in the (A) hyperpolarized and (B) depolarized states. A salt bridge is present if the minimum distance between the carboxyl oxygens of an acidic residue and the guanidino group of an arginine residue is smaller than 3.5 Å. pKa_1 and pKa_2 are the pH values that correspond to N_{hydr} at 1.5 and 0.5 respectively. (C) A schematic diagram showing the salt-bridge energy levels during the conformational activation of S4 from down (Hyperpol) up (Depol) states. The number 2 (pink), 3 (blue), and 4 (black) denote the numbers of salt bridges between gating charges in S4 and counter charges in S1 to S3.

Neutralization of D174 induces hydrophobic gasket wide opening

The calculated pK_a's of acids are all higher than 3.0, except for D174, the pK_a's of which in the hyperpolarized and depolarized states are 1.1 and 2.0 respectively (Tab. S2). Thus, D174 is titratable at the pH as low as 2.0 where other acids are basically protonated or neutralized. Therefore it's of interest to see whether the protonation of D174 participates in if any the response of Hv1 to extremely low pH condition. First, R_g of the hydrophobic gasket was calculated. Encouragingly, as illustrated in Fig. 6A, two peaks of R_g are found for the depolarized state. Whereas a single distribution of R_g around 6.2 Å is observed for the hyperpolarized state. Two states have similar distributions of R_g at pH=8. Nevertheless, for the depolarized state a new distribution around 7.5 Å emerges as pH reduces and dominates at pH=1. In addition, the salt bridges that concerns D174 were calculated and it's found that the minimum sidechain distances between D174 and K157 and between D174 and R226 in the depolarized state start to climb up as pH reduces to 3.0, in line with the pH-dependent transition of R_g. In contrast, the salt bridge D174-K157 stays intact even at pH=1.0 and the varying of R211-D174 appears irrelevant to the titration of D174 in the hyperpolarized state. As a consequence, we focus on the depolarized state next for the study of hHv1 reacting to extremely low inner pH condition since D174 locates at the intracellular side. As illustrate in Fig. 6B, R_g fluctuates around 7.5 Å when D174 is protonated at pH=1. On the other hand, when D174 is deprotonated at pH=3, most R_g values are distributed around 6.2 Å indicating that titration of D174 is coupled with the hydrophobic gasket wide opening.

Again, the correlation plots are utilized to address the connections between $r_{V177/178-F150}$ and R_g and between $r_{V177/178-F150}$ and Z_{S3}. As illustrated at the first column of Fig. 6C, Z_{S3} decreases as $r_{V177/178-F150}$. Mainly three states of the hydrophobic gasket were identified where state III corresponds to the wide opening of the hydrophobic gasket. To demonstrate the capability of $r_{V177/178-F150}$ to probe the hydrophobic gasket, the correlation between $r_{V177/178-F150}$ and R_g was calculated. From the second column of Fig. 6C, $r_{V177/178-F150}$ is positively related to R_g, in consistence with that in Fig. 2E. Thus our study suggests that when the salt bridge D174-K157 that links S2 to S3 is intact at the pH higher than 3, the hydrophobic interaction between F150 and V177/V178 as well as Z_{S3} is stabilized primarily in state I (Fig. 6D). Notably, state I with Z_{S3} around 2.0 Å is also sampled by the CpHMD simulation of hyperpolarized state especially when H168 is charged (state b in Fig. 2E). It's noticed that there is a minor intermediate state M (Fig. 6C pH=3 or 5), which might result from the less stabilized salt-bridge D174-R226 as illustrated in Fig. 6A. As pH reduces to 1.0 where D174 is largely protonated and D174-K157 is broken, states II and III dominate. In specific, F150 turns to interact with V109 in state II (Fig. 6D II and Fig. S6). Whereas in state III, the interaction between F150 and V109 is broken too (Fig. 6D III and Fig. S6), leading to wide opening of the hydrophobic gasket, which would facilitate the formation of a continuous water chain and therefore the proton transport. It should be highlighted that Z_{S3} decreases further in response to the increase of $r_{V177/178-F150}$, indicating that, apart from the above sandwish-like stacking, the salt-bridge interaction between D174 and K157 that locate in S3 and S2 respectively is another key regulator of the relative displacement between S3 and S2 and the resulting hydrophobic gasket opening.

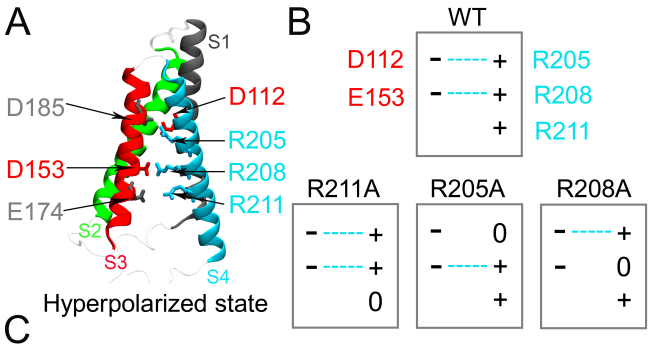

WT/Mutant	WT	R211A	R205A	R208A
N_Q	3	2	2	2
N_{SB}	2	2	1	1
ΔN	1	0	1	1
V_{thr} (mV)	7	77	6	14

Figure 5. (A) The structure of the hyperpolarized state. Among the pore-lining acids, D112 and D185 (red sticks) form stable salt bridges with gating charges R205 and R208 (cyan sticks) respectively. (B) Simplified representations of salt bridges formed by gating charges (R205, R208 and R211 in cyan) in S4 and counter charges in S1 to S3 (D112 and D185 in red) of wide type (WT) and three mutants R211A, R205A, and R208A. Salt bridges are marked with dashed cyan lines. (C) The number of gating charges (N_Q) as well as salt bridges (N_{SB}) are recorded in the table. ΔN equals N_Q minus N_{SB}. Threshold voltages (V_{thr}) with the unit of mV are extracted from literature[11].

Deprotonation of H140 facilitates inhibitive Zn^{2+} binding

To investigate whether the Zn^{2+} inhibition to hHv1 is pH dependent, we focus on the pK_a's of two putative Zn^{+} binding sites, namely H140 that lies at the outer half of S2 and H193 at the loop between S3 and S4[1]. Interestingly, the pK_a's of H140 are 5.3 and 6.9 in the hyperpolarized and depolarized states respectively, indicating distinct titrations of H140 (Fig. 7A). In particular, H140 is neutralized at the physiological pH (7.4) in the hyperpolarized state and its sidechain dihedral angle (χ_1) is found pH dependent. As illustrated in Fig. 7B, the probabilities of three rotamers of H140 sidechain in the hyperpolarized state as a function of pH are plotted. Apparently, the population of g- rotamer reduces as pH increases, whereas the ratio of trans rotamer varies in a opposite way, in consistence with the titration curve of H140 in the hyperpolarized state. As to g+ rotamer, it's rarely sampled. From Fig. 7C, one can see that H140 rotates down (trans rotamer) to interact with two hydrophobic residues, namely Y141 and I144 that locate on the same S2, which is responsible for pK_a shifting down and the resulting neutralization of H140 at the physiological pH. Taking into account the orientations of Y141 and I144 sidechains towards lipid tails, the trans rotamer makes H140 accessible to the hydrophobic lipid tails (See minimal distances between H140 and lipid:C in Fig. S7), which would contribute to the stabilization of the neutral state of H140. Once the sidechain rotates up (g- rotamer), the hydrophobic interaction is disrupted, allowing H140 to take a proton. Such a large fluctuation of H140 sidechain dihedral angle and its interaction with lipid bilayer agree with the previous fixed-charge MD simulations of hHv1[37].

As illustrated in Fig. 7A, the titration behaviors of H193 in both states are similar, implying that the protonation equilibra or pK_a value of H193 is not affected by the conformational change from the hyperpolarized (pK_a=8.4) to the depolarized state (pK_a=8.6). It's evident that H193 is fully protonated or charged at the physiological pH around 7.0. In contrast to H140, H193 is surrounded by two acidic residues, namely D123 and E192 (Fig. 7C), enabling H193 to take a proton under the pH as high as 8.0. Apart from the classic Coulomb and van der Waals forces, two Zn^{2+}-induced quantum effects, polarization and charge transfer, are crucial for the stability of the coordination sphere composed by deprotonated imidazole rings of histidines and carboxyls of aspatic or glutamic acids[46,47]. However, the Coulomb repulsive force between protonated or positively charged H193 and Zn^{2+} would exclude H193 from the coordination sphere. Thus our study proposes that different charge states employed by H140 and H193 causes a Zn^{2+} binding to H140 ahead of H193, which might explain the measured Zn^{2+} inhibition of H193A over H140A mutant[1].

Discussion

Recent experimental studies pointed out that Hv1 channels have distinct internal and external pH sensors and H168 has been identified as the pH_i sensor of hHv1[26,33]. However, the molecular mechanism of how H168 senses pH_i signal and the specific

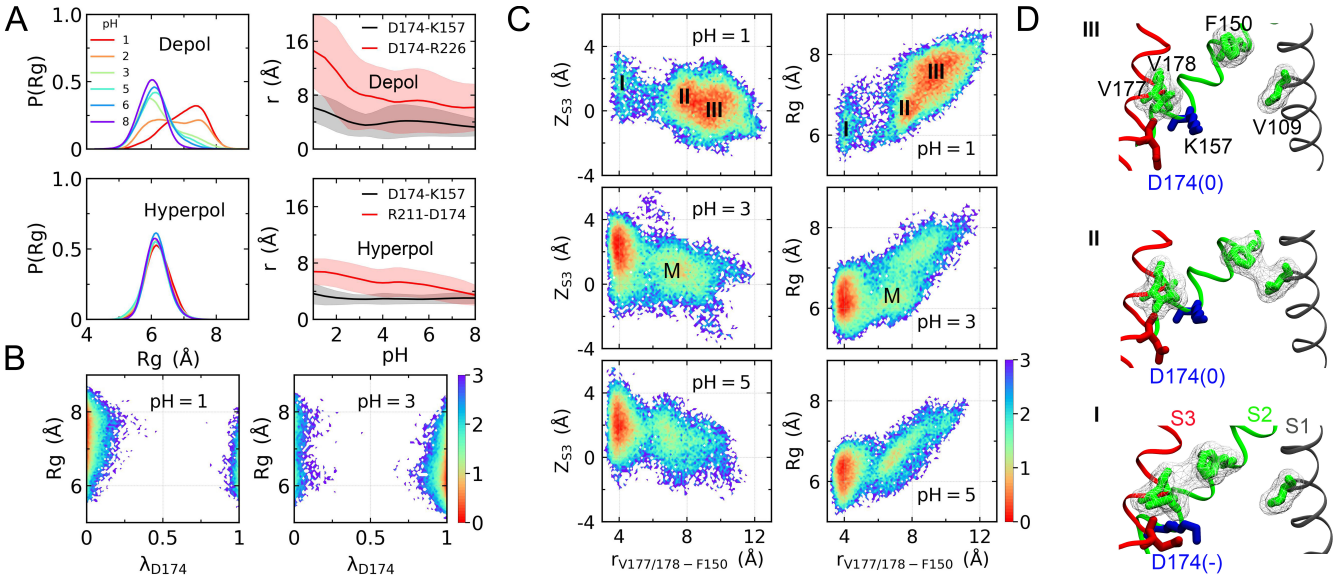

Figure 6. Titration of D174 is coupled with the hydrophobic gasket. (A) Radius of gyration (R_g) distributions of the hydrophobic gasket $P(R_g)$ and minimum distances between D174 and nearby bases as a function of pH for the depolarized (upside) and hyperpolarized (downside) states. (B) Correlation between titration coordinate of D174 ((λ_{D174})) and R_g at pH=1 and 3. (C) Correlations (left column) between minimum sidechain distance of F150 and V177/178 ($r_{V177/178-F150}$) and z-axis position of S3 (Z_{S3}) and (right column) between $r_{V177/178-F150}$ and R_g at pH =1, 3 and 5. (D) Snapshots showing closed (I), open (II) and wide open (III) states of the hydrophobic gasket composed by V109, F150, V177 and V178[35], which are represented with the stick combined with the wireframe mode. D174 (red) and K157 (blue) are displayed with the stick mode. Transmembrane helices S1, S2 and S3 are represented with the new ribbons mode.

residues responsible for pH_o dependence of hHv1 are still elusive. Our results support H168 as the internal sensor of hHv1. Notably, a salt bridge-aided sandwish-like stacking that blocks the simulated conformational activation of S3 has been identified to explain why the activation kinetics of hHv1 is slower than that of Hv1 in *Strongylocentrotus purpuratus*[26]. F161, R162 and H168 that form the sandwish-like stacking are well conserved[11,26]. In addition, E164 and E171 that contribute to the stabilization of the sandwish-like stacking via salt bridging with R162 sidechain are conserved too[11,26]. Thus, we propose that such an unique imidazole-centralized stacking is crucial for investigating pH_i dependence of hHv1. Apart from the reported mutations of H168, we assume that the mutation of F161 will to some extent disrupt the stacking and therefore reduce pH_i sensitivity of hHv1. According to the sequence alignment of voltage-gated domains, all residues for the stacking configuration above are present in the zebrafish Hv1, except for Y126, which corresponds to F161 in hHv1[11]. Thus, it's of interest to examine in future whether the single mutation of Y126F slows down the zebrafish Hv1. Regarding R162, E164 and D174, mutant R162A or E164A-D171A has been studied[11]. However the pH gradient is none-zero for R162A. Besides, solution and cell type for E164A-D171A differ from those for the wide type[11]. Thus, it's still worth examining whether the mutation R162A or E164A-D171A is able to accelerate the activation kinetics under the same experimental condition utilized by the wide type.

Regarding the pH_o dependence, E196 is predicted as the pH_o sensor. We propose that protonated E196 sidechain inserts into extracellular lipid tails and hinders the conformational activation of S4. Once hHv1 is activated, deprotonated E196 sidechain turns to interact with lipid heads, highlighting the active state stabilization by lipid head groups[48]. Thus we propose that the external pH that is a little higher than the physiological value is desired to accelerate the activation due to the deprotonation of E196. From the anit-cross correlation, we found that the titrations of H168 and E196 are coupled nearby the physiological pH condition. For instance, when H168 is charged, E196 is likely to be charged too, facilitating the conformational activations of S3 and S4. Taken together, we hypothesize that lower pH_i combined with higher pH_o will accelerate the activation kinetics of hHv1. From the experimental mean activation time constants (ms) as a function of voltage at different combinations of pH_i and pH_o, it's revealed that the combination of 7/7 (pH_i/pH_o) gives smaller time constant than 6/6 and 8/8[33], implying that the protonation states of pH_i and pH_o sensors that could accelerate the activation kinetics coexist at pH=7. Under the same ΔpH of 1, where $\Delta pH = pH_o - pH_i$), the time constant of 6/7 is smaller than that of 7/8[33], implying asymmetric effects of increasing pH_o and decreasing pH_i by 1.0 on the basis of 7/7. In our study, charged E196 and H168 coexist at pH=7, but with different populations. For instance, the probabilities of charged H196 and H168 are 0.3 and 0.1 respectively, meaning that the decrease of pH_i presumably by 1.0 is more desired, consistent with the time constant measurements above. So far as we know, single

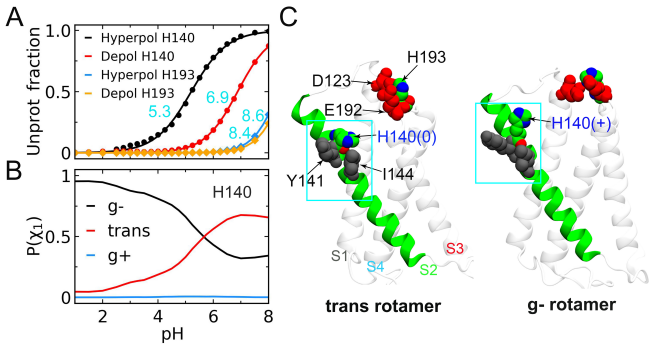

Figure 7. Sidechain dihedral fluctuation of H140. (A) Unprotonation fractions of H140 in the hyperpolarized (black) and depolarized (red) states and H193 in the hyperpolarized (blue) and depolarized (orange) states as a function of pH. (B) Probabilities of three rotamers, g^- (black), trans (red), and g^+ (blue), of H140 sidechain diehdral χ_1 as a function of pH. (C) Two snapshots showing trans and g^- rotamers of H140 sidechain diehdral χ_1. The protein is represented by the new cartoon mode. Residues of interest are displayed with the vdW surface mode.

mutation of E196, which is predicted by our study to reduce the threshold voltage, hasn't been reported. However, double mutations of E192 and E196, namely E192A-E196A, show small effect on the threshold voltage[11]. Based on our CpHMD simulation of the depolarized state, the salt-bridge probabilities of E192-R208 and E119-R208 are close, suggesting that E119A and E192A provide similar threshold voltages. Given the threshold votage of E119A (27 mV)[11], we hypothesize that the WT-like small threshold voltage by E192A-E196A is due to the compensated effects by E192A and E196A. Thus, to validate the pH_o-sensor role of E196, single mutation of E196 is demanded.

A main task of this study is to understand the mechanism underlying the measured threshold voltages of hHv1 mutants[1,11]. Based on the neutralizing mutations of three putative gating charges, we propose a salt bridge-based model, aiming at elucidating either the activation kinetics or statistics where the salt-bridge interaction between D174 and R211 (R211-D174) play the key role. It's found that the number of salt bridges in the simulated hyperpolarized state can vary between 2 and 3 because of the pH-dependent stability of R211-D174. Unlike D112, E153 involved salt bridge only appears in the hyperpolarized state, making the mutant E153A suitable for model testing. Intriguingly, the threshold voltage of E153A estimated by eq. 1 is -48 mV, in consistence with the measured value of -59 mV[11], validating the proposed model. Given the experimental threshold voltages of double mutants R205A/R208A and R205A/R211A, which are 135 and 108 mV respectively[11], the effective counts of salt bridges are predicted as 1.85 and 1.38 respectively. Here we assume that the remaining gating charges, R211 in R205A/R208A and R208 in R205A/R208A, form 2 and 1 salt bridges respectively with counter charges in S1 to S3, which requests future validation by experiment.

Given the depressed pK_a's of D174, we suggest that R211-D174 in the simulated hyperpolarized state nearby the physiological pH is disrupted by the above displacements of S3 or S4, rather than the protonation of D174. Nevertheless, once the channel is activated, neutralization of D174 disrupts the salt bridge K157-D174, which triggers downward displacement of S3 and the resulting hydrophobic gasket wide opening, the trend of which is consistent with that in the hyperpolarized state, highlighting the importance of S3 displacement during the process of activation. In addition to a key structural factor, our study suggests that titration of D174 is coupled with the function. From this view of point, D174 is more essential to the function of hHv1 than another four pore-lining acids D112, E119, E153 and D185 defined above, which explains larger threshold voltage amplitude of D174A (-104 mV) than D112A (66 mV), E119A (27 mV), E153A (-48 mV) and D185A (65 mV)[11]. Our CpHMD simulations reveal that the salt-bridge stability of R211-D112, R208-E119, R208-E153 or R211-D185 is pH independent in the physiological pH range, thus it's of interest to see if there is any relationship between measured threshold voltages and the simulated salt-bridge stabilities. Encouragingly, the threshold voltages of D112A, E119A, E153A and D185A with respect to that of WT (7 mV) become 59, 20, -55 and 58 mV respectively[11], the amplitudes of which are in line with the calculated probabilities of salt bridges R211-D112 ($\sim$ 1.0), R208-E119 ($\sim$ 0.5), R208-E153 ($\sim$ 1.0) and R211-D185 ($\sim$ 1.0) nearby physiological pH (5<pH<8). Further, it's noticed that when a pore-lining acid is mutated into a polar asparagine, rather than a nonpolar alanine, the corresponding threshold voltage is reduced. For instance, the changes are -28, -31 and -61 mv for D112, D174 and E153 respectively[11], indicating the acceleration of gating kinetics. From CpHMD simulations, a continuous water wire is observed when the pore-lining acids are neutralized, like asparagines (See snapshots with continuous water wires in Fig. S8). Thus we hypothesize that polar interactions between asparagine sidechains and pore water molecules facilitate proton conducting. On the contrary, hydrophobic alanines might lead to discontinuity of the aqueous medium for proton transfer. pK_a's of all pore-lining acids, except for D174, are close to the reference value of Asp (4.0) or Glu (4.4)[49]. Besides, the

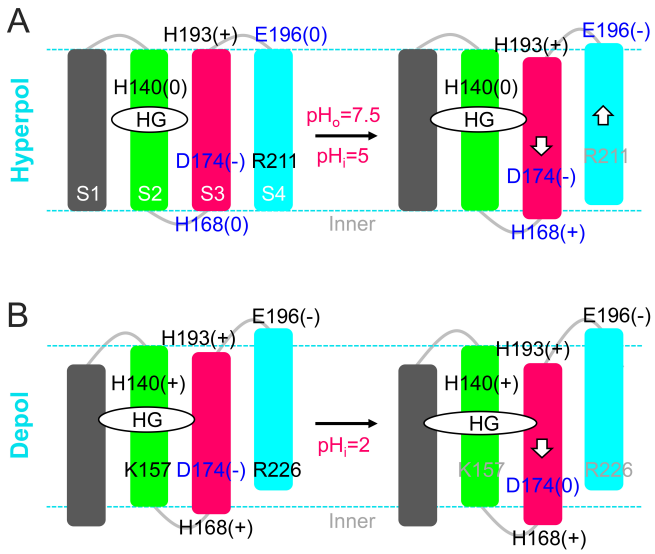

Figure 8. pH responses in the hyperpolarized and depolarized states. Simplified cartoons showing how hHv1 response to pH signal via titrations of some specific residues in the (A) hyperpolarized and (B) depolarized states. Four transmembrane helices S1 (gray), S2 (green), S3 (red) and S4 (cyan) are represented with rectangles. The links between two helices are shown with gray curves. Black open arrows are employed to indicate moving directions of S3 and S4 at membrane normal. HG is the abbreviation of hydrophobic gasket, which is represented by a ellipse. The widening of the ellipse indicates the opening of GH. When a salt bridge is broken, the color of a base involved fades. Besides, if the protonation state of a residue is changed in response to the pH noted, the residue is highlighted in blue. The charge state of a ionizable residue is displayed in a parenthesis.

calculated macroscopic pK_a's of D112 and D185 exclude them as proton carriers nearby physiological pH. Thus we assume that Grotthuss-type proton transfer along a continuous water chain is employed at extremely low (pH<3) or physiological (5<pH<8) pH range. Under the intermediate pH (3<pH<5), most pore-lining acids are titrated. Here we suggest that ionizable pore-lining acids themselves or combined with water molecules trapped in the pore provide a Grotthuss-like hopping chain for proton transfer[12,18,25].

The inhibitory effects of Zn^{2+} on Hv1 channels have been widely investigated in experiment and theory[38]. However, Zn^{2+} binding affinity in response to pH is rarely reported. According to the calculated pK_a's of two primary Zn^{2+} binding sites, H140 and H193, we propose that a Zn^{2+} binds to H140 first, because H193 is protonated at the physiological pH. In addition, we point out that once hHv1 is activated, H140 can be protonated as well due to the conformational change from the hyperpolarized to the depolarized state. Combined with the fact that Zn^{2+} inhibition is eliminated utterly by the mutation H140A/H193A[1], we predict that Zn^{2+} binding is weakened significantly upon activation where the two putative Zn^{2+} binding histidine sidechains are both protonated or positively charged. Apart from H140 and H193, E119, D123 and E192 have been implicated in Zn^{2+} binding[12,37,39]. Recently, two distinct Zn^{2+} binding spheres have been identified where one contains H140 and the other H193[13,37]. Here we come up with a pH-regulated Zn^{2+} binding pathway to the resting hHv1 channel. Initially, a Zn^{2+} is bound to H140. Next, two acids, presumably E119 and D123[12,50], are incorporated into the coordination sphere. As a result, the Zn^{2+} disrupts the electrostatic interaction between D123 and H193, leading to pK_a down shifting and the resulting deprotonation of H193, which is analogous to the competition between a sodium ion and a proton in the sodium-proton antiporter NhaA[27]. As the concentration of Zn^{2+} increases, deprotonation of H193 allows another Zn^{2+} to bind. Recently, membrane cholesterol was identified as a new inhibitor of hHv1[51]. In particular, cholesterol utilizes the same inhibitory mechanism with Zn^{2+}. Thus the present discussion on Zn^{2+} binding would shed light on future exploring the mechanism of cholesterol binding to hHv1.

In summary, we propose the following mechanism of pH sensing in hHv1. As illustrated in Fig. 8A, the channel initially stays in the hyperpolarized state. External E196 fluctuates between protonated (E196(0)) and deprotonated (E196(-)) states at pH$_o$=7.5 that is nearby the physiological pH. On the other hand, as pH$_i$ decreases to 5, both deprotonated (H168(0)) and protonated (H168(+)) states of internal H168 can be observed. Charged H168 and E196 trigger downward and upward movements of S3 and S4 respectively. As a result, the salt-bridge interaction between R211 and D174 is disrupted by the relative displacement between S3 and S4, which accelerates the gating kinetics as predicted by the salt bridge-based model above. Notably, the downward displacement of S3 is associated with the hydrophobic gasket (HG) opening. After the rate-limiting steps above, the newly sampled conformation, presumably an intermediate state of hHv1, can be stabilized by lipid head groups. Noting that H140 is neutralized around physiological pH, the channel will be inhibited once H140 is coordinated

with a Zn^{2+}. More details about Zn^{2+} inhibition that concerns H140 and H193 can be found in the above result section. As illustrated in Fig. 8B, the channel is activated. Notably, the initial position of S3 at membrane normal is close to that in the intermediate state above. Besides, H168 and E196 are stabilized in the charged state, resembling the intermediate state too. However, H140 becomes ionizable upon activation, which would prevent Zn^{2+} from binding. As pH_i reduces to 2, D174 becomes titratable. The salt bridge between K157 and D174 is stable when D174 is deprotonated (D174(-)). However, when D174 is protonated or neutralized (D174(0)), the salt bridge is broken, which is coupled with the downward displacement of S3 and the resulting hydrophobic gasket wide opening, facilitating protons conducting presumably by a continuous water chain. The pH values mentioned above are selected based on the pK_a values of H168 and E196 in the hyperpolarized state and D174 in the depolarized state where titration dynamics is coupled with conformational dynamics.

Methods

System preparation

The initial structures of monomeric hHv1 come from the hyperpolarized- and depolarized-state models of hHv1 obtained by Geragotelis and coworkers with 10-microsecond-timescale molecular dynamics simulations[21]. Membrane Builder module in the graphical user interface CHARMM-GUI was applied to create the simulation systems[52]. First, Orientations of Proteins in Membranes (OPM) was utilized to orientate the structures with respect to the membrane normal[53]. The truncated N (F88) and C (R230) terminals were capped with CH3CO (patch ACE) and NH2 (patch CT2) respectively. Default protonation states Asp(-)/Glu(-)/Lys(+)/Arg(+)/Cys(0)/His(0,HSD) under physiological pH (7.4) were used during the fixed-charge MD simulations. With respect to the continuous constant pH molecular dynamics (CpHMD) simulations, dummy hydrogen atoms were added to the carboxylate groups of acidic residues, Asp and Glu. Besides, HSD should be replaced with HSP, the protonated state of His. Either protein was inserted into a preassembled lipid bilayer, the length as well as the width of which was set 80Å. As a result, 84/83 and 81/80 1-palmitoyl-2-oleoyl-sn-glycero-3- phosphocholine (POPC) lipids were added to the upperleaflet and lowerleaflet respectively for the hyperpolarized or depolarized state[21]. A water layer of 15Å thickness was added to both sides of the lipid bilayer. In addition, 15 and 17 pore water molecules were added for the hyperpolarized and depolarized states respectively. 24 sodium and 33 chloride ions for the hyperpolarized state or 21 sodium and 30 choride ions for the depolarized state were added to neutralize the simulation box and to reach the physiological ionic strength of 0.15M. The final systems contain about 50,000 atoms. CHARMM22/CMAP force field was employed to describe the proteins[54,55], whereas lipids and ions were described by the CHARMM36 force field[56]. CHARMM modified TIP3P model was used to represent water.

Lipid equilibration

The positions of lipids were relaxed following the multi-step protocol in CHARMM-GUI[52]. After the initial equilibration, each protein-membrane complex was subject to a 200-ns fixed-charge MD simulation in the NPT ensemble where protein heavy atoms were restrained with a harmonic force constant of 1.0 kcal/mol/Å^2. Hoover thermostat method was employed to maintain the temperature of 310K. Langevin piston coupling method was utilized to keep the pressure constant at 1atm. The MD simulations were performed using the GPU-accelerated OpenMM[57]. The particle mesh Ewald method was used to calculate long-range electrostatics[58]. The real-space cutoff is 12Å and the reciprocal space calculation uses a 1-Å grid spacing and sixth-order spline interpolation. The SHAKE algorithm was used to constrain bonds involving hydrogen to enable a time step of 2 fs. Area per lipid (APL) and lipid order parameter(S_{CH}) were used to examine the convergences. APL can be calculated with GridMAT-MD[59]. S_{CH} as expressed in eq. 2 denotes the rigidity of the lipid tails and can be computed with a Tcl script for VMD[60]. From Fig. S9, one can see that the lipid bilayer with respect to either the hyperpolarized or depolarized state is stabilized after a 200-ns equilibration.

$$S_{CH} = \frac{1}{2}\langle 3cos^2\Theta - 1\rangle, \tag{2}$$

where Θ is the angle between the C-H bond of the lipid tail methylene and the membrane normal. The angular brackets denotes ensemble average.

CpHMD simulations

The CpHMD simulations were performed using CHARMM package (version c45a1)[61] and started from the final frames of the fixed-charge MD simulations above. The membrane-enabled hybrid-solvent CpHMD model was applied. The implicit low-dielectric membrane thickness and the radius of high-dielectric cylinder were set as 33Å and 12Å respectively[62]. The MMFP facility in CHARMM was employed to add a harmonic force to the center of mass of the protein where the force constant was 1.0 kcal/mol/Å^2[62]. The present work focuses on the titrations of those conserved Asp, Glu and His residues,

neutralizing mutations of which cause large shifts of the threshold voltage. Thus all Asp, Glu and His sidechains were allowed to titrate. Lys and Arg residues were fixed in protonated or charged state. However, to exclude the possible influence from the titration of Lys, in the second round Lys residues were set ionizable.

Single-pH (pH=7) CpHMD simulations were carried out to relax protein heavy atoms by removing the restraining forces gradually. The protein-membrane systems were equilibrated for another 1 ns in the NPT ensemble without any restraint. To improve the sampling of titration as well as conformational dynamics during the production simulations, pH-based replica-exchange protocol was employed[63]. Now that Arg and Lys residues with higher standard pK_a's, 10.4 and 12.5 respectively[49], were fixed in charged state during the first round, the pH range was 1.0-8.0 with a total of 24 replicas and the specific pH conditions were 1.0, 1.5, 2.0, 2.5, 2.75, 3.0, 3.5, 3.25, 3.75, 4.0, 4.25, 4.5, 4.75, 5.0, 5.25, 5.5, 5.75, 6.0, 6.25, 6.5, 6.75, 7.0, 7.5, and 8.0. Notably, the pH intervals nearby the reference pK_a's of Asp (4.0), Glu (4.4) and His (6.5)[49] were reduced by half to smooth the replica-exchange ratios across the pH replicas. Extremely low-pH replicas were applied such that the neutral state of a Asp or Glu residue involved in salt bridges or hydrogen bonds could be sampled. The simulation for each replica lasted 30 ns. In the second round, to have the deprotonated state of Lys sampled, pH conditions distribute from 3.0 to 11.5 with the interval of 0.5. As a result, there are 16 replicas in total and the running length each is 20 ns. Notably, two adjacent replicas were attempted to exchange every 500 MD steps or 1 ps. Each round contains two CpHMD simulations, so the accumulated running length of four CpHMD simulations reaches 2.08 microseconds. According to the root-mean-square deviations as given in Fig. S10, the first 8 ns was discarded for final data analyses.

Analysis

The pK_a value of a specific residue was calculated by fitting the unprotonated fraction (S) to the generalized Henderson-Hasselbalch equation,

$$S(\mathrm{pH}) = \frac{1}{1+10^{n(\mathrm{pK_a}-\mathrm{pH})}}, \tag{3}$$

where n is the Hill coefficient. The macroscopic sequential pK_a's of two coupled titrating residues were obtained by fitting the time-averaged number of protons (N_{proton}) bound to the two sites to the model[64],

$$N_{\mathrm{proton}}(\mathrm{pH}) = \frac{10^{\mathrm{p}K_2-\mathrm{pH}} + 2\times 10^{\mathrm{p}K_1+\mathrm{p}K_2-2\mathrm{pH}}}{1+10^{\mathrm{p}K_2-\mathrm{pH}} + 10^{\mathrm{p}K_1+\mathrm{p}K_2-2\mathrm{pH}}}, \tag{4}$$

where pK_1 and pK_2 are the two sequential pK_a's. The correlation (R) between two titration events under a pH condition can be calculated with the normalized cross-correlation function[64],

$$R_{xy}(\Delta t) = \frac{1}{N}\sum_{i=1}^{N}\frac{[x(i)-\bar{x}][(y(i)+\Delta t)-\bar{y}]}{\sigma_x\sigma_y}, \tag{5}$$

where x and y denote the titration coordinates of two coupled titrating sites. Δt is an offset of time. $\bar{x}$ and $\bar{y}$ are the population means and σ is the standard deviation. N is the total number of data points. R ranges from -1 to 1 that represent completely anti-correlated and correlated respectively.

Radius of gyration (eq. 6) was employed to assess the openness of the hydrophobic gasket, side chains of V109, F150, V177 and V178[35].

$$R_g = \sqrt{\frac{\sum_{i=1}^{N} m_i r_i^2}{\sum_{i=1}^{N} m_i}}, \tag{6}$$

where m_i and r_i denotes the mass of atom i in the hydrophobic gasket and the distance of the atom from the center of mass of the hydrophobic gasket. N is the total number of atoms.

References

1. Ramsey, I. S., Moran, M. M., Chong, J. A. & Clapham, D. E. A voltage-gated proton-selective channel lacking the pore domain. *Nature* **440**, 1213–1216 (2006).
2. Sasaki, M., Takag, M. & Okamura, Y. A voltage sensor–domain protein is a voltage-gated proton channel. *Science* **312**, 589–592 (2006).

3. Decoursey, T. E. Voltage-gated proton channels and other proton transfer pathways. *Physiol. Rev.* **83**, 475–579 (2003).

4. Musset, B. *et al.* Aspartate 112 is the selectivity filter of the human voltage-gated proton channel. *Nature* **480**, 273–277 (2011).

5. Wu, L. *et al.* The voltage-gated proton channel Hv1 enhances brain damage from ischemic stroke. *Nat. Neurosci.* **15**, 565–573 (2012).

6. Lishko, P. V., Botchkina, I. L., Fedorenko, A. & Kirichok, Y. Acid extrusion from human spermatozoa is mediated by flagellar voltage-gated proton channel. *Cell* **140**, 327–337 (2010).

7. Capasso, M. *et al.* HVCN1 modulates BCR signal strength via regulation of BCRdependent generation of reactive oxygen species. *Nat Immunol* **11**, 265–272 (2010).

8. Lishko, P. V., Botchkina, I. L., Fedorenko, A. & Kirichok, Y. Acid extrusion from human spermatozoa is mediated by flagellar voltage-gated proton channel. *Cell* **140**, 327–337 (2010).

9. He, J., Ritzel, R. M. & Wu, J. Functions and mechanisms of the voltage-gated proton channel Hv1 in brain and spinal cord injury. *Front. Cell. Neurosci.* **15**, 662971 (2021).

10. DeCoursey, T. E., Morgan, D., Musset, B. & Cherny, V. V. nsights into the structure and function of HV1 from a meta-analysis of mutation studies. *J. Gen. Physiol.* **148**, 97–118 (2016).

11. Ramsey, I. S. *et al.* An aqueous H^+ permeation pathway in the voltage-gated proton channel Hv1. *Nat. Struct. Mol. Biol.* **17**, 869–875 (2010).

12. Takeshita, K. *et al.* X-ray crystal structure of voltage-gated proton channel. *Nat. Struct. Mol. Biol.* **21**, 352–357 (2014).

13. Bayrhuber, M. *et al.* Nuclear Magnetic Resonance Solution Structure and Functional Behavior of the Human Proton Channel. *Biochemistry* **58**, 4017–4027 (2019).

14. Wood, M. L. *et al.* Water wires in atomistic models of the Hv1 proton channel. *Biochimica et Biophys. Acta* **1818**, 286–293 (2012).

15. Kulleperuma, K. *et al.* Construction and validation of a homology model of the human voltage-gated proton channel hHV1. *J. Gen. Physiol.* **141**, 445–465 (2013).

16. Chamberlin, A. *et al.* Hydrophobic plug functions as a gate in voltage-gated proton channels. *Proc. Natl. Acad. Sci. U. S. A.* **30**, E273–E282 (2013).

17. Gianti, E., Delemotte, L., Klein, M. L. & Carneval, V. On the role of water density fluctuations in the inhibition of a proton channel. *Proc. Natl. Acad. Sci. U. S. A.* **113**, E8359–E8368 (2016).

18. van Keulen, S. C. *et al.* Does proton conduction in the voltage-gated H+ channel hHv1 involve Grotthuss-like hopping via acidic residues? *J. Phys. Chem. B* **121**, 3340–3351 (2017).

19. Lee, M., Bai, C., Feliks, M., Alhadeff, R. & Warshel, A. On the control of the proton current in the voltage-gated proton channel Hv1. *Proc. Natl. Acad. Sci. U. S. A.* **115**, 10321–10326 (2018).

20. Li, Q. *et al.* Resting state of the human proton channel dimer in a lipid bilayer. *Proc. Natl. Acad. Sci. U. S. A.* **112**, E5926–E5935 (2015).

21. Geragotelis, A. D. *et al.* Voltage-dependent structural models of the human Hv1 proton channel from long-timescale molecular dynamics simulations. *Proc. Natl. Acad. Sci. U. S. A.* **117**, 13490–13498 (2020).

22. Jardin, C., Ohlwein, N., Franzen, A., Chaves, G. & Musset, B. The pH-dependent gating of the human voltage-gated proton channel from computational simulations. *Phys. Chem. Chem. Phys.* **24**, 9964–9977 (2022).

23. Swails, J. M., York, D. M. & Roitberg, A. E. Constant pH Replica Exchange Molecular Dynamics in Explicit Solvent Using Discrete Protonation States: Implementation, Testing, and Validation. *J. Chem. Theory Comput.* **10**, 1341–1352 (2014).

24. Nguyen, H., Roe, D. R. & Simmerling, C. Improved Generalized Born Solvent Model Parameters for Protein Simulations. *J. Chem. Theory Comput.* **9**, 2020–2034 (2013).

25. Boytsov, D. *et al.* Trapped pore waters in the open proton channel HV1. *BioRxiv* DOI: https://doi.org/10.1101/2022.05.09.491141 (2022).

26. Cherny, V. V. *et al.* Histidine^{168} is crucial for ΔpH-dependent gating of the human voltage-gated proton channel, hH_v1. *J. Gen. Physiol.* **180**, 851–862 (2018).

27. Huang, Y., Chen, W., Dotson, D. L., Beckstein, O. & Shen, J. Mechanism of pH-dependent activation of the sodium-proton antiporter NhaA. *Nat. Commun.* **7**, 12940 (2016).

28. Henderson, J. A., Huang, Y., Beckstein, O. & Jana, S. Alternative Proton-Binding Site and Long-Distance Coupling in *Escherichia Coli* Sodium–Proton Antiporter NhaA. *Proc. Natl. Acad. Sci. USA* **117**, 25517–25522 (2020).

29. Chen, W., Huang, Y. & Shen, J. Conformational Activation of a Transmembrane Proton Channel from Constant pH Molecular Dynamics. *J. Phys. Chem. Lett.* **7**, 3961–3966 (2016).

30. Yue, Z., Chen, W., Zgurskaya, H. I. & Shen, J. Constant pH Molecular Dynamics Reveals How Proton Release Drives the Conformational Transition of a Transmembrane Efflux Pump. *J. Chem. Theory Comput.* **13**, 6405–6414 (2017).

31. Vo, Q. N., Mahinthichaichan, P., Shen, J. & Ellis, C. R. How μ-opioid receptor recognizes fentanyl. *Nat. Commun.* **12**, 984 (2021).

32. DeCoursey, T. E. Voltage and pH sensing by the voltage-gated proton channel, Hv1. *J. R. Soc. Interface* **15**, 20180108 (2018).

33. Carmonan, E. M. *et al.* The voltage sensor is responsible for ΔpH dependence in H_V1 channels. *Proc. Natl. Acad. Sci. U. S. A.* **118**, e2025556118 (2021).

34. Koch, H. P. *et al.* Multimeric nature of voltage-gated proton channels. *Proc. Natl. Acad. Sci. U. S. A.* **105**, 9111–9116 (2008).

35. Banh, R. *et al.* Hydrophobic gasket mutation produces gating porecurrents in closed human voltage-gatedproton channels. *Proc. Natl. Acad. Sci. U. S. A.* **116**, 18951–18961 (2019).

36. Qiu, F. *et al.* Molecular mechanism of Zn^{2+} inhibition of avoltage-gated proton channel. *Proc. Natl. Acad. Sci. U. S. A.* **113**, E5962–E5971 (2016).

37. Jardin, C., Chaves, G. & Musset, B. Assessing structural determinants of Zn^{2+} binding ot human H_V1 via multiple MD simulations. *Biophys. J.* **118**, 1221–1233 (2020).

38. Larsson, H. P. Zn^{2+} to probe voltage-gated proton (Hv1) channels. *J. Gen. Physiol.* **152**, e202012725 (2020).

39. Iwaki, M. *et al.* Zn^{2+}-Binding to the Voltage-Gated Proton Channel Hv1/VSOP. *J. Phys. Chem. B* **122**, 9076–9080 (2018).

40. DeCoursey, T. E. CrossTalk proposal: proton permeation through Hv1 requires transient protonation of a conserved aspartate in the S1 transmembrane helix. *J. Physiol.* **595**, 6793–6795 (2017).

41. Bennett, A. L. & Ramsey, I. S. CrossTalk opposing view: proton transfer in Hv1 utilizes a water wire, and does not require transient protonation of a conserved aspartate in the S1 transmembrane helix. *J. Physiol.* **595**, 6797–6799 (2017).

42. Dudev, T. *et al.* Selectivity mechanism of the voltage-gated proton channel, Hv1. *Sci. Reports* **5**, 10320 (2015).

43. Randolph, A. L., Mokrab, Y., Bennett, A. L., Sansom, M. S. & Ramsey, I. S. Proton currents constrain structural models of voltage sensor activation. *eLife* **5**, e18017 (2016).

44. Liao, S., Du, Q., Meng, J., Pang, Z. & Huang, R. The multiple roles of histidine in protein interactions. *Chem. Cent. J.* **7**, 44 (2013).

45. Loof, H. D., Nilsson, L. & Rigler, R. Molecular dynamics simulation of galanin in aqueous and nonaqueous solution. *J. Am. Chem. Soc.* **114**, 4028–4035 (1992).

46. Sakharov, D. V. & Lim, C. Zn Protein Simulations Including Charge Transfer and Local Polarization Effects. *J. Am. Chem. Soc.* **127**, 4921–4929 (2005).

47. Huang, Y. & Shuai, J. Induced dipoles incorporated into all-atom Zn protein simulations with multiscale modeling. *J. Phys. Chem. B* **117**, 6138–6148 (2013).

48. Schmidt, D., Jiang, Q. & MacKinnon, R. Phospholipids and the origin of cationic gating charges in voltage sensors. *Nature* **444**, 775–779 (2006).

49. Nozaki, Y. & Tanford, C. Examination of titration behavior. *Methods Enzym.* **11**, 715–734 (1967).

50. Okamura, Y., Fujiwara, Y. & Sakata, S. Gating mechanisms of voltage-gated proton channels. *Annu. Rev. Biochem.* **84**, 685–709 (2015).

51. Han, S. *et al.* Cholesterol inhibits human voltage-gated proton channel hHv1. *Proc. Natl. Acad. Sci. U. S. A.* **119**, e2205420119 (2022).

52. Jo, S., Kim, T. & Im, W. Automated builder and database of protein/membrane complexes for molecular dynamics simulations. *PLoS ONE* **2**, e880 (2007).

53. Lomize, M. A., Lomize, A. L., Pogozheva, I. D. & Mosberg, H. I. OPM: orientations of proteins in membranes database. *Bioinformatics* **22**, 623–625 (2006).

54. MacKerell, Jr., A. D. *et al.* All-atom empirical potential for molecular modeling and dynamics studies of proteins. *J. Phys. Chem. B* **102**, 3586–3616 (1998).

55. MacKerell, Jr., A. D., Feig, M. & Brooks, III, C. L. Extending the treatment of backbone energetics in protein force fields: limitations of gas-phase quantum mechanics in reproducing protein conformational distributions in molecular dynamics simulations. *J. Comput. Chem.* **25**, 1400–1415 (2004).

56. Klauda, J. B. *et al.* Update of the CHARMM all-atom additive force field for lipids: validation on six lipid types. *J. Phys. Chem. B* **114**, 7830–7843 (2010).

57. Eastman, P. *et al.* OpenMM 7: Rapid development of high performance algorithms for molecular dynamics. *PLoS Comput. Biol.* **13**, e1005659 (2017).

58. Darden, T., York, D. & Pedersen, L. Particle mesh Ewald: An N log(N) method for Ewald sums in large systems. *J. Chem. Phys.* **98**, 10089–10092 (1993).

59. Allen, W., Lemkul, J. & Bevan, D. GridMAT-MD: A grid-based membrane analysis tool for use with molecular dynamics. *J. Comput. Chem.* **30**, 1952–1958 (2009).

60. Humphrey, W., Dalke, A. & Schulten, K. VMD: visual molecular dynamics. *J. Mol. Graph.* **14**, 33–38 (1996).

61. Brooks, B. *et al.* Charmm: the biomolecular simulation program. *J. Comput. Chem.* **30**, 1545–1614 (2009).

62. Huang, Y., Henderson, J. A. & Shen, J. Continuous Constant pH Molecular Dynamics Simulations of Transmembrane Proteins. *Methods Mol. Biol.* **2302**, 275–287 (2021).

63. Wallace, J. A. & Shen, J. K. Continuous constant pH molecular dynamics in explicit solvent with pH-based replica exchange. *J. Chem. Theory Comput.* **7**, 2617–2629 (2011).

64. Wallace, J. A. & Shen, J. K. Charge-leveling and proper treatment of long-range electrostatics in all-atom molecular dynamics at constant pH. *J. Chem. Phys.* **137**, 184105 (2012).

Acknowledgements

Y.H. acknowledges the financial support by the National Natural Science Foundation of China (11804114) and the National Key R&D Program of China (2018YFD0901004).

Author contributions

Y.H. and J.S. conceived the research. Y.H. performed the MD and CpHMD simulations. Y.H., Z.C., T.L. and J.S. analysed the results. Y.H. and J.S. wrote the paper.

Data availability

All necessary data are available in the manuscript and supporting information. Additional raw data are available upon request.